Available online at www.sciencedirect.com
SCIENCE DIRECT
Journal of Computational Physics 215 (2006) 133–152
JOURNAL OF COMPUTATIONAL PHYSICS
www.elsevier.com/locate/jcp

A lattice Boltzmann algorithm for calculation of the laminar jet diffusion flame

Taehun Lee [a], Ching-Long Lin [a,*], Lea-Der Chen [b]

[a] Department of Mechanical and Industrial Engineering, IIHR – Hydroscience & Engineering, The University of Iowa, Iowa City, IA 52242-1527, USA
[b] Department of Mechanical and Industrial Engineering, The National Advanced Driving Simulator, The University of Iowa, Iowa City, IA 52242-1527, USA

Received 30 November 2004; received in revised form 21 June 2005; accepted 27 October 2005
Available online 9 December 2005

Abstract

A new two-distribution lattice Boltzmann equation (LBE) algorithm is presented to solve the laminar diffusion flames within the context of Burke–Schumann flame sheet model. One distribution models the transport of the Schvab–Zeldovich coupling function, or the mixture fraction to combine the energy and species equations. The other distribution models the quasi-incompressible Navier–Stokes equations with the low Mach number approximation. In the quasi-incompressible flows, the thermodynamics quantities depend on the coupling function but not on the hydrodynamic pressure, and the fluid components are assumed to be compressible only in the mixing/reaction region. A systematic and consistent approach to deriving LBEs for the general advection–diffusion equation and the quasi-incompressible Navier–Stokes equations are also presented. The streaming step of the LBEs are discretized by the total variation diminishing (TVD) Lax–Wendroff scheme. Numerical simulations are carried out to reproduce the low frequency flame oscillation (or flame flicker) of buoyant jet diffusion flame. Comparison between the quasi-incompressible model and the incompressible model is presented and the role of non-solenoidal velocity is examined.

Keywords: Lattice Boltzmann equation; Laminar diffusion flame; Quasi-incompressible flow; TVD scheme

1. Introduction

The lattice Boltzmann equation (LBE) method is based on microscopic models and mesoscopic kinetic equations [1]. Even though the major focus is the averaged macroscopic behavior, its kinetic nature can provide many of the advantages of molecular dynamics, especially the near wall treatment at micro-fluid level [2],. This implies that the LBE method could be a useful tool for understanding mesoscopic combustion phenomena in complex geometries. However, research on LBE algorithms for combustion problems has been limited

* Corresponding author. Tel.: +1 319 335 5673; fax: +1 319 335 5669.
E-mail addresses: thlee@ccny.cuny.edu (T. Lee), ching-long-lin@uiowa.edu (C.-L. Lin), lea-der-chen@uiowa.edu (L.-D. Chen).

0021-9991/$ - see front matter © 2005 Elsevier Inc. All rights reserved.
doi:10.1016/j.jcp.2005.10.021

and started only recently. The principal difficulty could be attributed to the fact that the original LBE method is valid in the incompressible limit and nearly constant density case. Severe density variation could violate Galilean invariance of the LBE method.

The first lattice Boltzmann equation simulation of combustion problems was carried out by Succi et al. [3] under the assumptions of fast chemistry and *cold* flames with weak heat release. As a result of the latter assumption, density variation was not allowed in the model. Yamamoto et al. [4] presented a LBE method for reaction, diffusion, and convection based on the incompressible LBE model of [5,6]. In addition to incompressibility of the fluids, they assumed that the chemical reaction did not affect the flow field. Therefore, density variation was allowed but not considered in the solution of the momentum equation. Filippova and Hänel [7,8] proposed the LBE model for reacting flows at low Mach number, which allowed density variation in the flow field due to temperature changes over a significant dynamical range of values. It contained the modified lattice BGK [9] model for the solution of the continuity and momentum equations and a finite-difference method for the transport equations of temperature and species. In [7,8], the LBE model was derived by modifying the equilibrium distribution function such that the modified LBE could recover the desired momentum equation without non-Galilean invariant terms. Time derivative of density was added to the stationary particle distribution function in order to recover the continuity equation. From the authors' experience, the time derivative of density triggers numerical instability, when the variation of density is not small.

In the present paper, a two-distribution LBE algorithm is presented to solve the unsteady Burke–Schumann diffusion flame. One distribution models the transport of the Schvab–Zeldovich coupling function, or the mixture fraction to combine the energy and species equations. The other distribution models the Navier–Stokes equations. The major assumptions are negligible radiative heat transfer and viscous dissipation, low Mach number, and laminar Newtonian flow. A flame-sheet model is used to calculate the thermodynamical properties of the flame [10]. The flame-sheet model assumes an infinitely large Damköhler number (i.e., fast chemistry), equal diffusion coefficients for all species, and a unity Lewis number for the mixture. A state relationship between mixture fraction and properties such as density and temperature is also assumed.

The present derivation is based on the body force approach of He et al. [11] that was originally proposed to model the discrete Boltzmann equation for non-ideal gases. Their LBE recovers the Navier–Stokes equations for liquid–vapor two-phase flows. Later, more useful formulation was proposed by He et al. [12]. They transformed the compressible LBE into the incompressible LBE by redefining a new particle distribution function and removing terms related to the divergence of velocity. The transform is extended to derivation of the quasi-incompressible flow in the present study. A systematic and consistent approach to deriving LBEs for transport of the mixture fraction is also presented. Since the derivation is valid for any unsteady advection–diffusion equation, it is equally applicable to finite-rate chemistry problems, although the current LBE is derived for fast chemistry problems.

The paper is organized as follows. In Section 2, the macroscopic governing equations for the Burke–Schumann diffusion flame with low Mach number approximation are presented. In Section 3, the DBEs (discrete Boltzmann equations) for the transport of the mixture fraction and the momentum are derived in a consistent manner. In Section 4, discretization of the DBEs is presented. We will show that the resulting LBEs thus obtained are indeed second-order accurate. The monotonicity preserving TVD Lax–Wendroff scheme is also described in Section 4. The proposed algorithm is tested for the Burke–Schumann diffusion flame in Section 5. Numerical simulations are carried out to reproduce the flicker frequency of buoyant jet diffusion flame. The quasi-incompressible solution is compared with the incompressible solution. Section 6 is concluding remarks.

2. Macroscopic equations with low Mach number approximation

The mathematical formulation of the macroscopic governing equations is based on the time-dependent variable density flow in two-dimensional Cartesian coordinate system. The major assumptions are negligible radiative heat transfer and viscous dissipation, low Mach number, and laminar Newtonian flow. Based on these assumptions, the numerical model is supposed to solve the transport equations for the conservation of scalar (i.e., mixture fraction ϕ in the study), mass, and momentum [10].

Mixture fraction

$$\frac{\partial(\rho\phi)}{\partial t}+\frac{\partial(\rho\phi u_j)}{\partial x_j}=\frac{\partial}{\partial x_j}\left(\rho\mathscr{D}\frac{\partial\phi}{\partial x_j}\right). \tag{1}$$

Continuity

$$\frac{\partial\rho}{\partial t}+\frac{\partial(\rho u_j)}{\partial x_j}=0. \tag{2}$$

Momentum

$$\frac{\partial(\rho u_i)}{\partial t}+\frac{\partial(\rho u_i u_j)}{\partial x_j}=-\frac{\partial P}{\partial x_i}+\frac{\partial}{\partial x_j}\left[\mu\left(\frac{\partial u_i}{\partial x_j}+\frac{\partial u_j}{\partial x_i}\right)\right]+\rho g_i. \tag{3}$$

Ideal gas equation of state

$$p^{(\mathrm{t})}=\rho RT=p^{(\mathrm{t})}(t), \tag{4}$$

where ρ and $\mathbf{u}$ are the density and velocity of the mixture, respectively. ϕ is the mixture fraction which will be defined later, μ is the dynamic viscosity, $p^{(\mathrm{t})}$ the thermodynamic pressure, ρg_i the gravitational force, and $\mathscr{D}$ the diffusion coefficient. R is the gas constant and T is the temperature.

The pressure-like variable P can be written as $P=p^{(\mathrm{h})}+\frac{2}{3}\mu\frac{\partial u_k}{\partial x_k}\delta_{ij}$, $p^{(\mathrm{h})}$ being the hydrodynamic pressure. For low Mach number flow in an unconfined domain, the low Mach number approximation assumes that the fluctuating pressure field, $p^{(\mathrm{h})}/p^{(\mathrm{t})}\sim \mathrm{O}(Ma^2)$, where Ma is the Mach number, and that all thermodynamic quantities are independent of $p^{(\mathrm{h})}$ [13]. This flow is referred to as the "quasi-incompressible" flow. In the quasi-incompressible flow, the fluids components are assumed to be compressible only in the mixing region [14]. In absence of temperature gradients, the Navier–Stokes equations in the low Mach number limit reduces to the Navier–Stokes equations for the incompressible flow [8]. The linear deformation of the quasi-incompressible fluids can be expressed in terms of diffusion of the mixture fraction rather than unsteady advection of the density, because the density is no longer a function of the hydrodynamic pressure, but a function of the mixture fraction.

A flame-sheet model is used to calculate the thermodynamical properties of the flame [10]. The flame-sheet model assumes an infinitely large Damköhler number (i.e., fast chemistry), equal diffusion coefficients for all species, and a unity Lewis number for the mixture. It is further assumed that the flame is adiabatic, and a one-step irreversible chemical reaction occurs in an infinitely thin region with CO_2 and H_2O being the only combustion products. With these assumptions, the Shvab–Zeldovich formulation [25] can be used; namely, a single conserved scalar, or the mixture fraction, is used to combine the energy and species equations. The mixture fraction is defined as

$$\phi=\frac{[b]_m-[b]_{\mathrm{O}_\infty}}{[b]_{\mathrm{F}_\infty}-[b]_{\mathrm{O}_\infty}} \tag{5}$$

or

$$\phi=\frac{[H]_m-[H]_{\mathrm{O}_\infty}}{[H]_{\mathrm{F}_\infty}-[H]_{\mathrm{O}_\infty}}, \tag{6}$$

where subscripts m, O_∞, and F_∞ denote the local mixture condition, the oxidant stream at $\mathbf{x}=\infty$, and the fuel stream at $\mathbf{x}=\infty$, respectively. Parameters b and H are defined as

$$b=Y_{\mathrm{F}}-(F/O)_{\mathrm{st}}Y_{\mathrm{O}}, \tag{7}$$

where F/O denotes the fuel oxidant ratio, subscript st stands for the stoichiometric condition and Y_i is the mass fraction of species i,

$$H=h+\sum_{i=1}^{N}Y_i\Delta h^0_{f,i}, \tag{8}$$

where $h = \int_{T_0}^{T} c_p \, dT$ and $\Delta h_{f,i}^0$ is the thermal enthalpy and the standard state enthalpy of formulation of ith species, respectively.

The divergence of the velocity can be obtained from the continuity equation, i.e.,

$$\frac{\partial u_i}{\partial x_i} = -\frac{1}{\rho}\left(\frac{\partial \rho}{\partial t} + u_i \frac{\partial \rho}{\partial x_i}\right). \tag{9}$$

The thermodynamic quantities such as the density and the temperature can be expressed as functions of the mixture fraction ϕ [26]. Employing the conserved scalar approach, one can evaluate the density variation as follows:

$$\frac{\partial \rho}{\partial t} = \frac{d\rho}{d\phi}\frac{\partial \phi}{\partial t} \tag{10}$$

and

$$\frac{\partial \rho}{\partial x_i} = \frac{d\rho}{d\phi}\frac{\partial \phi}{\partial x_i}. \tag{11}$$

Substituting Eqs. (10) and (11) into Eq. (9), one obtains [27]

$$\frac{\partial u_i}{\partial x_i} = -\frac{1}{\rho^2}\frac{d\rho}{d\phi}\frac{\partial}{\partial x_i}\left(\rho \mathscr{D}\frac{\partial \phi}{\partial x_i}\right) \tag{12}$$

in which $d\rho/d\phi$ can be either analytically or numerically calculated. The role of the pressure-like variable is now to satisfy Eq. (12). Hereafter, P will be called the pressure for simplicity.

3. Discrete Boltzmann equation for the laminar diffusion flame

3.1. Discrete Boltzmann equation with external body force

The Boltzmann equation with the BGK collision model can be written as [11]

$$\frac{\partial f}{\partial t} + \xi_i \frac{\partial f}{\partial x_i} + F_i \frac{\partial f}{\partial \xi} = -\frac{f - f^{eq}}{\lambda}, \tag{13}$$

where $f \equiv f(x, \xi_i, t)$ is the particle distribution function in the phase space $f \equiv f(x, \xi_i)$, ξ_i is the microscopic velocity, F_i is an external body force, λ is the relaxation parameter due to collision, and f^{eq} is the Maxwell–Boltzmann distribution function.

Since the derivative $\partial_\xi f$ cannot be calculated directly, He et al. [11] take the leading part of the distribution function and approximate the derivative as

$$\frac{\partial f}{\partial \xi} \approx \frac{\partial f^{eq}}{\partial \xi} = -\frac{\xi_i - u_i}{c_s^2} f^{eq}. \tag{14}$$

With this approximation, discretization of the microscopic velocity field ξ on unit lattice now yields the discrete Boltzmann equation with discretized microscopic velocity e_α ($\alpha = 0, 1, 2, \ldots, B$)

$$\frac{Df_\alpha}{Dt} = \frac{\partial f_\alpha}{\partial t} + e_{\alpha i}\frac{\partial f_\alpha}{\partial x_i} = -\frac{f_\alpha - f_\alpha^{eq}}{\lambda} + \frac{(e_{\alpha i} - u_i)F_i}{c_s^2} f^{eq}, \tag{15}$$

where B is the number of discretized velocity. The equilibrium distribution function is given as [28]

$$f_\alpha^{eq} = t_\alpha \rho\left[1 + \frac{e_{\alpha i}u_i}{c_s^2} + \frac{\left(e_{\alpha i}e_{\alpha j} - c_s^2\delta_{ij}\right)u_i u_j}{2c_s^4}\right], \tag{16}$$

where t_α is a weighting factor. The relaxation parameter is given as $\lambda = \mu/\rho c_s^2$ in which the mixture density ρ and the mixture viscosity μ are calculated from the mixture fraction ϕ.

For $F_i = \rho g_i$, where ρg_i is the gravitational force, the recovered macroscopic governing equations from Eq. (15) are

$$\frac{\partial \rho}{\partial t} + \frac{\partial(\rho u_i)}{\partial x_i} = 0, \tag{17}$$

$$\frac{\partial(\rho u_i)}{\partial t} + \frac{\partial(\rho u_i u_j)}{\partial x_j} = -\frac{\partial c_s^2 \rho}{\partial x_i} + \frac{\partial}{\partial x_j}\left[\mu\left(\frac{\partial u_i}{\partial x_j} + \frac{\partial u_j}{\partial x_i}\right)\right] + \rho g_i. \tag{18}$$

3.2. Discrete Boltzmann equation for momentum transport

In the conventional LBE method that is valid for the isothermal ideal gas flows, $c_s^2\rho = p^{(t)}$. Since the thermodynamic pressure $p^{(t)}$ is assumed constant in the present case, $c_s^2\rho$ can no longer represent the pressure. Thus, we consider an additional body force term $\tilde{F}_i$ which restores Eq. (18) to Eq. (3). An admissible choice of $\tilde{F}_i$ might be $\tilde{F}_i = \partial_i(c_s^2\rho) - \partial_i P$. Adding $\tilde{F}_i$ to Eq. (15) yields

$$\frac{\partial f_\alpha}{\partial t} + e_{\alpha i}\frac{\partial f_\alpha}{\partial x_i} = -\frac{f_\alpha - f_\alpha^{eq}}{\lambda} + \frac{(e_{\alpha i} - u_i)(\tilde{F}_i + F_i)}{c_s^2\rho} f^{eq} = -\frac{f_\alpha - f_\alpha^{eq}}{\lambda} + \frac{(e_{\alpha i} - u_i)[\partial_i(c_s^2\rho) - \partial_i P + \rho g_i]}{c_s^2\rho} f^{eq}. \tag{19}$$

Eq. (19) recovers the continuity equation (2) and the momentum equation (3) through the Chapman–Enskog expansion. Nevertheless, Eq. (19) cannot be used to obtain the pressure since zeroth moment of the particle distribution function f_α is the density, not the pressure. The density is to be obtained from the mixture fraction, as will be discussed later. In order to transform Eq. (19) into the equation for the pressure and the velocity, we follow the transform proposed by He et al. [12].

A new variable is introduced, whose zeroth moment is the pressure by design. We define a particle distribution function g_α as

$$g_\alpha = c_s^2 f_\alpha + \left(P - c_s^2\rho\right)\Gamma_\alpha(0), \tag{20}$$

where $\Gamma_\alpha(\mathbf{u}) = f_\alpha^{eq}/\rho$. By substituting g_α into Eq. (19), the evolution equation for g_α is obtained as:

$$\begin{aligned}\frac{Dg_\alpha}{Dt} &= c_s^2\frac{Df_\alpha}{Dt} + \frac{DP}{Dt}\Gamma(0) - c_s^2\frac{D\rho}{Dt}\Gamma(0)\\ &= -\frac{1}{\lambda}\left(g_\alpha - g_\alpha^{eq}\right) + (e_{\alpha i} - u_i)\left[\frac{\partial}{\partial x_i}\left(\rho c_s^2 - P\right) + \rho g_i\right]\Gamma(\mathbf{u}) + \frac{DP}{Dt}\Gamma(0) - c_s^2\frac{D\rho}{Dt}\Gamma(0),\end{aligned} \tag{21}$$

where the new equilibrium g_α^{eq} is

$$g_\alpha^{eq} = t_\alpha\left[P + \rho c_s^2\left(\frac{e_{\alpha i}u_i}{c_s^2} + \frac{\left(e_{\alpha i}e_{\alpha j} - c_s^2\delta_{ij}\right)u_i u_j}{2c_s^4}\right)\right]. \tag{22}$$

The last two terms on the right-hand side (RHS) of Eq. (21) can be expanded through the continuity equation as follows. We assume

$$\frac{DP}{Dt} = \frac{\partial P}{\partial t} + e_{\alpha i}\frac{\partial P}{\partial x_i} \approx e_{\alpha i}\partial_i P, \tag{23}$$

where $\partial_t P$ becomes on the order of the truncation error in the low frequency limit [8]. Note that P is $\mathcal{O}(Ma^2)$, and thus the product of P and $\mathbf{u}$ will be $\mathcal{O}(Ma^3)$. The total derivative of the density becomes

$$\frac{D\rho}{Dt} = \frac{\partial \rho}{\partial t} + e_{\alpha i}\frac{\partial \rho}{\partial x_i} = (e_{\alpha i} - u_i)\frac{\partial \rho}{\partial x_i} - \rho\frac{\partial u_i}{\partial x_i}. \tag{24}$$

Substitution of Eq. (12) into Eq. (24) yields

$$\frac{D\rho}{Dt} = \frac{\partial \rho}{\partial t} + e_{\alpha i}\frac{\partial \rho}{\partial x_i} = (e_{\alpha i} - u_i)\frac{\partial \rho}{\partial x_i} + \frac{1}{\rho}\frac{d\rho}{d\phi}\frac{\partial}{\partial x_i}\left(\rho\mathscr{D}\frac{\partial \phi}{\partial x_i}\right). \tag{25}$$

There are a couple of differences between the present derivation and that in [12]. He et al. [12] set $D_t P$ to zero in Eq. (21), because they assumed that P is a function of the density and the material derivative of any function of the density is zero for incompressible fluids. Due to zero divergence, Eq. (24) reduces to

$$\frac{\mathrm{D}\rho}{\mathrm{D}t} = \frac{\partial\rho}{\partial t} + e_{\alpha i}\frac{\partial\rho}{\partial x_i} = (e_{\alpha i} - u_i)\frac{\partial\rho}{\partial x_i}. \tag{26}$$

In Section 5, the LBE model based on Eq. (26) will be referred to as "incompressible model", while the LBE model based on Eq. (24) as "quasi-incompressible model". They are different only in the mixing region.

Finally, Eqs. (23) and (24) are substituted into the DBE for g_α, yielding

$$\frac{\partial g_\alpha}{\partial t} + e_{\alpha i}\frac{\partial g_\alpha}{\partial x_i} = -\frac{1}{\lambda}\left(g_\alpha - g_\alpha^{\mathrm{eq}}\right) + (e_{\alpha i} - u_i)\frac{\partial\rho c_{\mathrm{s}}^2}{\partial x_i}(\Gamma(\mathbf{u}) - \Gamma(0)) - \frac{c_{\mathrm{s}}^2}{\rho}\frac{\mathrm{d}\rho}{\mathrm{d}\phi}\frac{\partial}{\partial x_i}\left(\rho\mathscr{D}\frac{\partial\phi}{\partial x_i}\right)\Gamma(0) + \rho g_i\Gamma(\mathbf{u}). \tag{27}$$

The macroscopic variables are calculated by

$$P = \sum_{\alpha=0}^{B} g_\alpha, \quad c_{\mathrm{s}}^2\rho u_i = \sum_{\alpha=1}^{B} e_{\alpha i} g_\alpha. \tag{28}$$

Eq. (27) recovers the macroscopic transport equations for the quasi-incompressible flow:

$$\frac{1}{\rho c_{\mathrm{s}}^2}\frac{\partial P}{\partial t} + \frac{\partial u_i}{\partial x_i} = -\frac{1}{\rho^2}\frac{\mathrm{d}\rho}{\mathrm{d}\phi}\frac{\partial}{\partial x_i}\left(\rho\mathscr{D}\frac{\partial\phi}{\partial x_i}\right), \tag{29}$$

$$\frac{\partial(\rho u_i)}{\partial t} + \frac{\partial(\rho u_i u_j)}{\partial x_j} = -\frac{\partial P}{\partial x_i} + \frac{\partial}{\partial x_j}\left[\mu\left(\frac{\partial u_i}{\partial x_j} + \frac{\partial u_j}{\partial x_i}\right)\right] + \rho g_i. \tag{30}$$

In the low frequency limit, the time derivative of P becomes negligible and divergence of the velocity approximately satisfies Eq. (12).

It is noteworthy that the LBE of Yamamoto et al. [4] recovers the following equation for the pressure:

$$\frac{1}{\rho_\infty c_{\mathrm{s}}^2}\frac{\partial P}{\partial t} + \frac{\partial u_i}{\partial x_i} = 0, \tag{31}$$

while the LBE of Filippova and Hänel [7,8] recovers

$$\frac{1}{c_{\mathrm{s}}^2}\frac{\partial P}{\partial t} + \frac{\partial\rho}{\partial t} + \frac{\partial(\rho u_i)}{\partial x_i} = 0, \tag{32}$$

which in terms of divergence of the velocity can be recast as

$$\frac{1}{\rho c_{\mathrm{s}}^2}\frac{\partial P}{\partial t} + \frac{\partial u_i}{\partial x_i} = -\frac{1}{\rho}\left(\frac{\partial\rho}{\partial t} + u_i\frac{\partial\rho}{\partial x_i}\right). \tag{33}$$

Although Eq. (33) is generally valid for the compressible flow, stability concern arising from numerical treatment of $\partial_t\rho$ on the RHS is not trivial.

3.3. Discrete Boltzmann equation for scalar transport

There are several ways of choosing a distribution function for the mixture fraction, but here we choose $h_\alpha = \phi f_\alpha$. This choice satisfies the following conditions of the equilibrium distribution for the mixture fraction h_α^{eq} [29]:

$$\begin{aligned}
&\sum_{\alpha=1}^{B} e_{\alpha i} f_\alpha^{\mathrm{eq}} = \rho u_i,\\
&\sum_{\alpha=0}^{B} h_\alpha = \sum_{\alpha=0}^{B} h_\alpha^{\mathrm{eq}} = \rho\phi,\\
&\sum_{\alpha=1}^{B} e_{\alpha i} h_\alpha = \sum_{\alpha=1}^{B} e_{\alpha i} h_\alpha^{\mathrm{eq}} = \rho\phi u_i.
\end{aligned} \tag{34}$$

The equilibrium distribution is determined such that the above conditions are satisfied

$$h_\alpha^{\mathrm{eq}} = \phi f_\alpha^{\mathrm{eq}} = t_\alpha \rho \phi \left[1 + \frac{e_{\alpha i}u_i}{c_s^2} + \frac{(e_{\alpha i}e_{\alpha j} - c_s^2\delta_{ij})u_i u_j}{2c_s^4}\right]. \tag{35}$$

Taking the total derivative D_t of the new variable h_α and utilizing Eq. (19) yield

$$\frac{\mathrm{D}h_\alpha}{\mathrm{D}t} = \phi\frac{\mathrm{D}f_\alpha}{\mathrm{D}t} + f_\alpha\frac{\mathrm{D}\phi}{\mathrm{D}t} = -\frac{1}{\lambda}(h_\alpha - h_\alpha^{\mathrm{eq}}) + \frac{(e_{\alpha i} - u_i)(\partial_i \rho c_s^2 + \rho g_i) - e_{\alpha i}\partial_i P}{c_s^2 \rho} h^{\mathrm{eq}} + \left(\frac{\partial\phi}{\partial t} + e_{\alpha i}\frac{\partial\phi}{\partial x_i}\right) f_\alpha, \tag{36}$$

where $u_i\partial_i P \sim \mathcal{O}(Ma^3)$ is neglected. The last term on the RHS can be expanded as

$$\left(\frac{\partial\phi}{\partial t} + e_{\alpha i}\frac{\partial\phi}{\partial x_i}\right) f_\alpha = \left[(e_{\alpha i} - u_i)\frac{\partial\phi}{\partial x_i} + \frac{1}{\rho}\frac{\partial}{\partial x_i}\left(\rho\mathscr{D}\frac{\partial\phi}{\partial x_i}\right)\right] f_\alpha. \tag{37}$$

As is assumed to approximate the external body force term in [11], f_α in Eq. (37) is approximated by f_α^{eq}. Making use of Eq. (37) with this approximation leads to a DBE for the transport of the mixture fraction:

$$\frac{\partial h_\alpha}{\partial t} + e_{\alpha i}\frac{\partial h_\alpha}{\partial x_i} = -\frac{1}{\lambda}(h_\alpha - h_\alpha^{\mathrm{eq}}) + (e_{\alpha i} - u_i)\left[\frac{\partial(\rho\phi)}{\partial x_i} + \frac{\rho\phi}{c_s^2}g_i\right]\Gamma(\mathbf{u}) - e_{\alpha i}\frac{\phi}{c_s^2}\frac{\partial P}{\partial x_i}\Gamma(\mathbf{u}) + \frac{\partial}{\partial x_i}\left(\rho\mathscr{D}\frac{\partial\phi}{\partial x_i}\right)\Gamma(\mathbf{u}) \tag{38}$$

which recovers Eq. (1) through the Chapman–Enskog expansion.

4. Discretization of the discrete Boltzmann equations

4.1. Lattice Boltzmann equations

In order to numerically solve the DBEs, Eqs. (27) and (38), we discretize these equations along characteristics over time step δt. The LBE for g_α is obtained

$$\begin{aligned} g_\alpha(\mathbf{x} + \mathbf{e}_\alpha\delta t, t + \delta t) - g_\alpha(\mathbf{x}, t) = &-\int_t^{t+\delta t}\left[\frac{g_\alpha - g_\alpha^{\mathrm{eq}}}{\lambda}\right]\mathrm{d}t + \int_t^{t+\delta t}\left[(e_{\alpha i} - u_i)\frac{\partial\rho c_s^2}{\partial x_i}(\Gamma(\mathbf{u}) - \Gamma(0))\right]\mathrm{d}t \\ &- \int_t^{t+\delta t}\left[\frac{c_s^2}{\rho}\frac{\mathrm{d}\rho}{\mathrm{d}\phi}\frac{\partial}{\partial x_i}\left(\rho\mathscr{D}\frac{\partial\phi}{\partial x_i}\right)\Gamma(0) - \rho g_i\Gamma(\mathbf{u})\right]\mathrm{d}t. \end{aligned} \tag{39}$$

Note that the time integration in $[t, t + \delta t]$ is coupled with the space integration in $[\mathbf{x}, \mathbf{x} + \mathbf{e}_\alpha\delta t]$. The Chapman–Enskog analysis shows that the trapezoidal rule must be used for the integration in order not to introduce any spurious derivatives of the second term into the system while retaining second-order accuracy [15]. Application of the trapezoidal rule leads to

$$\begin{aligned} g_\alpha(\mathbf{x} + \mathbf{e}_\alpha\delta t, t + \delta t) - g_\alpha(\mathbf{x}, t) = &-\left[\frac{g_\alpha - g_\alpha^{\mathrm{eq}}}{2\tau}\right]_{(\mathbf{x},t)} - \left[\frac{g_\alpha - g_\alpha^{\mathrm{eq}}}{2\tau}\right]_{(\mathbf{x}+\mathbf{e}_\alpha\delta t, t+\delta t)} \\ &+ \frac{\delta t}{2}\left[(e_{\alpha i} - u_i)\frac{\partial\rho c_s^2}{\partial x_i}(\Gamma(\mathbf{u}) - \Gamma(0))\right]_{(\mathbf{x},t)} \\ &+ \frac{\delta t}{2}\left[(e_{\alpha i} - u_i)\frac{\partial\rho c_s^2}{\partial x_i}(\Gamma(\mathbf{u}) - \Gamma(0))\right]_{(\mathbf{x}+\mathbf{e}_\alpha\delta t, t+\delta t)} \\ &- \frac{\delta t}{2}\left[\frac{c_s^2}{\rho}\frac{\mathrm{d}\rho}{\mathrm{d}\phi}\frac{\partial}{\partial x_i}\left(\rho\mathscr{D}\frac{\partial\phi}{\partial x_i}\right)\Gamma(0) - \rho g_i\Gamma(\mathbf{u})\right]_{(\mathbf{x},t)} \\ &- \frac{\delta t}{2}\left[\frac{c_s^2}{\rho}\frac{\mathrm{d}\rho}{\mathrm{d}\phi}\frac{\partial}{\partial x_i}\left(\rho\mathscr{D}\frac{\partial\phi}{\partial x_i}\right)\Gamma(0) - \rho g_i\Gamma(\mathbf{u})\right]_{(\mathbf{x}+\mathbf{e}_\alpha\delta t, t+\delta t)}, \end{aligned} \tag{40}$$

where $\tau = \lambda/\delta t$.

Likewise, the LBE for h_α is

$$\begin{aligned} h_\alpha(\mathbf{x}+\mathbf{e}_\alpha\delta t, t+\delta t) - h_\alpha(\mathbf{x},t) = &-\left[\frac{h_\alpha - h_\alpha^{\mathrm{eq}}}{2\tau}\right]_{(\mathbf{x},t)} - \left[\frac{h_\alpha - h_\alpha^{\mathrm{eq}}}{2\tau}\right]_{(\mathbf{x}+\mathbf{e}_\alpha\delta t, t+\delta t)} \\ &+\frac{\delta t}{2}\left[(e_{\alpha i}-u_i)\left[\frac{\partial(\rho\phi)}{\partial x_i}+\frac{\rho\phi}{c_s^2}g_i\right]\Gamma(\mathbf{u}) - e_{\alpha i}\frac{\phi}{c_s^2}\frac{\partial P}{\partial x_i}\Gamma(\mathbf{u}) + \frac{\partial}{\partial x_i}\left(\rho\mathscr{D}\frac{\partial\phi}{\partial x_i}\right)\Gamma(\mathbf{u})\right]_{(\mathbf{x},t)} \\ &+\frac{\delta t}{2}\left[(e_{\alpha i}-u_i)\left[\frac{\partial(\rho\phi)}{\partial x_i}+\frac{\rho\phi}{c_s^2}g_i\right]\Gamma(\mathbf{u}) - e_{\alpha i}\frac{\phi}{c_s^2}\frac{\partial P}{\partial x_i}\Gamma(\mathbf{u}) + \frac{\partial}{\partial x_i}\left(\rho\mathscr{D}\frac{\partial\phi}{\partial x_i}\right)\Gamma(\mathbf{u})\right]_{(\mathbf{x}+\mathbf{e}_\alpha\delta t, t+\delta t)} \\ &+\frac{\delta t}{2}\left[\frac{\partial}{\partial x_i}\left(\rho\mathscr{D}\frac{\partial\phi}{\partial x_i}\right)\Gamma(\mathbf{u})\right]_{(\mathbf{x},t)} + \frac{\delta t}{2}\left[\frac{\partial}{\partial x_i}\left(\rho\mathscr{D}\frac{\partial\phi}{\partial x_i}\right)\Gamma(\mathbf{u})\right]_{(\mathbf{x}+\mathbf{e}_\alpha\delta t, t+\delta t)}. \end{aligned} \tag{41}$$

The above LBEs can be solved in three steps as shown in [19]. In the present study, however, we introduce new variables to facilitate computations. If we define $\bar{g}_\alpha$ and $\bar{h}_\alpha$ such that

$$\bar{g}_\alpha = g_\alpha + \frac{g_\alpha - g_\alpha^{\mathrm{eq}}}{2\tau} - \frac{\delta t}{2}\left[(e_{\alpha i}-u_i)\frac{\partial\rho c_s^2}{\partial x_i}(\Gamma(\mathbf{u})-\Gamma(0)) - \frac{c_s^2}{\rho}\frac{\mathrm{d}\rho}{\mathrm{d}\phi}\frac{\partial}{\partial x_i}\left(\rho\mathscr{D}\frac{\partial\phi}{\partial x_i}\right)\Gamma(0) + \rho g_i\Gamma(\mathbf{u})\right]_{(\mathbf{x},t)} \tag{42}$$

and

$$\bar{h}_\alpha = h_\alpha + \frac{h_\alpha - h_\alpha^{\mathrm{eq}}}{2\tau} - \frac{\delta t}{2}\left[(e_{\alpha i}-u_i)\left[\frac{\partial(\rho\phi)}{\partial x_i}+\frac{\rho\phi}{c_s^2}g_i\right]\Gamma(\mathbf{u}) - e_{\alpha i}\frac{\phi}{c_s^2}\frac{\partial P}{\partial x_i}\Gamma(\mathbf{u}) + \frac{\partial}{\partial x_i}\left(\rho\mathscr{D}\frac{\partial\phi}{\partial x_i}\right)\Gamma(\mathbf{u})\right]_{(\mathbf{x},t)}. \tag{43}$$

Now, Eqs. (40) and (41) are solved in simpler two steps:

Collision step

$$\begin{aligned} \bar{g}_\alpha(\mathbf{x},t) := \bar{g}_\alpha(\mathbf{x},t) &- \left[\frac{\bar{g}_\alpha - g_\alpha^{\mathrm{eq}}}{\tau+0.5}\right]_{(\mathbf{x},t)} \\ &+\frac{\tau\delta t}{\tau+0.5}\left[(e_{\alpha i}-u_i)\frac{\partial\rho c_s^2}{\partial x_i}(\Gamma(\mathbf{u})-\Gamma(0)) - \frac{c_s^2}{\rho}\frac{\mathrm{d}\rho}{\mathrm{d}\phi}\frac{\partial}{\partial x_i}\left(\rho\mathscr{D}\frac{\partial\phi}{\partial x_i}\right)\Gamma(0) + \rho g_i\Gamma(\mathbf{u})\right]_{(\mathbf{x},t)}, \end{aligned} \tag{44}$$

$$\begin{aligned} \bar{h}_\alpha(\mathbf{x},t) := \bar{h}_\alpha(\mathbf{x},t) &- \left[\frac{\bar{h}_\alpha - h_\alpha^{\mathrm{eq}}}{\tau+0.5}\right]_{(\mathbf{x},t)} \\ &+\frac{\tau\delta t}{\tau+0.5}\left[(e_{\alpha i}-u_i)\left[\frac{\partial(\rho\phi)}{\partial x_i}+\frac{\rho\phi}{c_s^2}g_i\right]\Gamma(\mathbf{u}) - e_\alpha\frac{\phi}{c_s^2}\frac{\partial P}{\partial x_i}\Gamma(\mathbf{u}) + \frac{\partial}{\partial x_i}\left(\rho\mathscr{D}\frac{\partial\phi}{\partial x_i}\right)\Gamma(\mathbf{u})\right]_{(\mathbf{x},t)}. \end{aligned} \tag{45}$$

Streaming step

$$\bar{g}_\alpha(\mathbf{x}+\mathbf{e}_\alpha\delta t, t+\delta t) = \bar{g}_\alpha(\mathbf{x},t), \tag{46}$$

$$\bar{h}_\alpha(\mathbf{x}+\mathbf{e}_\alpha\delta t, t+\delta t) = \bar{h}_\alpha(\mathbf{x},t). \tag{47}$$

The mixture fraction, the velocity, and the pressure are calculated below after the streaming step

$$\rho\phi = \sum_\alpha \bar{h}_\alpha + \frac{\delta t}{2}\frac{\partial}{\partial x_i}\left(\rho\mathscr{D}\frac{\partial\phi}{\partial x_i}\right), \tag{48}$$

$$\rho c_s^2 u_i = \sum_\alpha \mathbf{e}_\alpha\bar{g}_\alpha + \frac{c_s^2\delta t}{2}\rho g_i, \tag{49}$$

$$P = \sum_\alpha \bar{g}_\alpha + \frac{c_s^2\delta t}{2}u_i\frac{\partial\rho}{\partial x_i} - \frac{\delta t}{2}\frac{c_s^2}{\rho}\frac{\mathrm{d}\rho}{\mathrm{d}\phi}\frac{\partial}{\partial x_i}\left(\rho\mathscr{D}\frac{\partial\phi}{\partial x_i}\right). \tag{50}$$

The density is easily calculated from $\rho\phi$ by solving a quadratic equation (see Appendix A). However, obtaining $\rho\phi$ using Eq. (48) requires implicit calculation. In this study, we explicitly take this value at the previous time step. Accuracy and stability of the explicit treatment of source terms is analyzed in Appendix B.

4.2. TVD Lax–Wendroff discretization

The Lagrangian description of the streaming step in the LBE given by Eqs. (46) and (47) can alternatively be expressed in an Eulerian framework shown below [19].

$$\frac{\partial \bar{g}_\alpha}{\partial t} + e_{\alpha i}\frac{\partial \bar{g}_\alpha}{\partial x_i} = 0, \tag{51}$$

$$\frac{\partial \bar{h}_\alpha}{\partial t} + e_{\alpha i}\frac{\partial \bar{h}_\alpha}{\partial x_i} = 0. \tag{52}$$

The above streaming step can be solved by virtually any second-order accurate schemes suited for the pure advection equation. On uniform structured mesh, spatial gradients in Eqs. (51) and (52) can be projected along the characteristics to yield a system of one-dimensional pure advection equations. To improve the accuracy associated with truncation error in the discretization of the advection equations, smaller time-step and/or finer mesh resolutions are usually used. An alternative is to adopt a higher-order accurate numerical scheme. Unfortunately, the higher-order accurate schemes (i.e., order higher than one) are also known for the tendency to produce nonphysical dispersions or oscillations in the solution [10]. The numerical diffusion and oscillation errors can artificially suppress or amplify the instabilities in an unsteady or time-dependent flow; thus, it may overwhelm the physics of the fluid flow or the heat transfer being studied. Therefore, the robustness of a numerical model is of particular importance to the simulation of time-dependent flow.

In general, the LBE method with consistent discretization yields second-order accurate solution in time and space [1]. The perfect shift in the conventional LBE method, however, is only neutrally stable and numerical disturbances may produce nonphysical oscillations in solution. The Lax–Wendroff scheme [16] has been applied to the streaming step in place of the perfect shift [17–19] in an effort to stabilize the otherwise unstable LBE method. In fact, the Lax–Wendroff LBE method is a natural extension of the conventional LBE method in that the direct application of Taylor series expansion to the conventional LBE up to second-order leads to the Lax–Wendroff formulation for space centered discretization [19]. Even though the Lax–Wendroff LBE method usually works well for single-phase flows, it is not entirely free from the nonphysical oscillations especially for multi-phase or reactive flows in which spatial gradients of the thermodynamical quantities are generally large. The Warming and Beam scheme [20] improves stability and reduces the nonphysical oscillations over the Lax–Wendroff scheme, but still is not enough for multi-phase/reactive flows, for which monotonicity preserving [22] schemes are required.

The TVD LBE scheme, which is monotonicity preserving, has been proposed by Teng et al. [23]. They applied the TVD space discretization directly to the discrete Boltzmann equation (DBE) and used the second-order Runge–Kutta time marching method. The source terms including the collision term and the body force terms are treated explicitly, which restricts the applicability of the scheme at high Reynolds number (Re) [19]. We propose to use a simpler TVD discretization based on the Lax–Wendroff scheme [24] (or Warming and Beam scheme). The TVD Lax–Wendroff scheme is applied to discretize the streaming step, which reduces to the Lax–Wendroff scheme in the region of smooth solutions and selectively becomes the Warming and Beam scheme depending on relative ratio of adjacent gradients. Overall accuracy of the scheme is second-order.

In the following sections, second-order accurate advection schemes are introduced and applied to the advection of the particle distribution functions.

4.2.1. Second-order space-centered and upwind schemes

There are two unique second-order accurate explicit schemes in both time and space on the support of three grid points in one-dimension [22].

4.2.1.1. Lax–Wendroff scheme. The one-dimensional Lax–Wendroff scheme [16] along the characteristics is the unique second-order space-centered discretization on the three-point support $(\mathbf{x} + e_\alpha \delta t_0, \mathbf{x}, \mathbf{x} - \mathbf{e}_\alpha \delta t_0)$, δt_0 being unit time step such that $\mathbf{e}_\alpha \delta t_0$ is the exact grid spacing along characteristics. It can be written as

$$\bar{g}_\alpha(\mathbf{x}, t+\delta t) - \bar{g}_\alpha(\mathbf{x}, t) = -\frac{\delta t}{2}[\bar{g}_\alpha(\mathbf{x}+\mathbf{e}_\alpha\delta t_0, t) - \bar{g}_\alpha(\mathbf{x}-\mathbf{e}_\alpha\delta t_0, t)] + \frac{\delta t^2}{2}[\bar{g}_\alpha(\mathbf{x}+\mathbf{e}_\alpha\delta t_0, t) - 2\bar{g}_\alpha(\mathbf{x}, t) + \bar{g}_\alpha(\mathbf{x}-\mathbf{e}_\alpha\delta t_0, t)]. \tag{53}$$

Eq. (53) can also be rewritten as a correction to the first-order upwind scheme

$$\bar{g}_\alpha(\mathbf{x}, t+\delta t) - \bar{g}_\alpha(\mathbf{x}, t) = -\delta t[\bar{g}_\alpha(\mathbf{x}, t) - \bar{g}_\alpha(\mathbf{x}-\mathbf{e}_\alpha\delta t_0, t)] - \frac{\delta t}{2}(1-\delta t)\delta^-[\bar{g}_\alpha(\mathbf{x}+\mathbf{e}_\alpha\delta t_0, t) - \bar{g}_\alpha(\mathbf{x}, t)], \tag{54}$$

where δ^- of any variable ψ is defined as $\delta^-\psi(\mathbf{x},t) = \psi(\mathbf{x}, t) - \psi(\mathbf{x}-\mathbf{e}_\alpha\delta t_0, t)$.

4.2.1.2. Warming and Beam scheme. The one-dimensional Warming and Beam scheme [20] along characteristics is the unique second-order upwind discretization on the three-point support $(\mathbf{x}, \mathbf{x}-e_\alpha\delta t_0, \mathbf{x}-2\mathbf{e}_\alpha\delta t_0)$ and can be written as

$$\bar{g}_\alpha(\mathbf{x}, t+\delta t) - \bar{g}_\alpha(\mathbf{x}, t) = -\frac{\delta t}{2}[3\bar{g}_\alpha(\mathbf{x}, t) - 4\bar{g}_\alpha(\mathbf{x}-\mathbf{e}_\alpha\delta t_0, t) + \bar{g}_\alpha(\mathbf{x}-2\mathbf{e}_\alpha\delta t_0, t)] + \frac{\delta t^2}{2}[\bar{g}_\alpha(\mathbf{x}, t) - 2\bar{g}_\alpha(\mathbf{x}-\mathbf{e}_\alpha\delta t_0, t) + \bar{g}_\alpha(\mathbf{x}-2\mathbf{e}_\alpha\delta t_0, t)]. \tag{55}$$

Again Eq. (55) can be rewritten as a correction to the first-order upwind scheme

$$\bar{g}_\alpha(\mathbf{x}, t+\delta t) - \bar{g}_\alpha(\mathbf{x}, t) = -\delta t[\bar{g}_\alpha(\mathbf{x}, t) - \bar{g}_\alpha(\mathbf{x}-\mathbf{e}_\alpha\delta t_0, t)] - \frac{\delta t}{2}(1-\delta t)\delta^-[\bar{g}_\alpha(\mathbf{x}, t) - \bar{g}_\alpha(\mathbf{x}-\mathbf{e}_\alpha\delta t_0, t)]. \tag{56}$$

In the case of unit time step, i.e., $\delta t = \delta t_0 = 1$, both the Lax–Wendroff scheme and the Warming and Beam scheme reduce to the perfect shift commonly used in the conventional LBE method. Any linear second-order accurate explicit scheme on the support $(\mathbf{x} + e_\alpha\delta t_0, \mathbf{x}, \mathbf{x}-\mathbf{e}_\alpha\delta t_0, \mathbf{x}-2\mathbf{e}_\alpha\delta t_0)$ can be obtained as a linear combination of the Lax–Wendroff and the Warming and Beam scheme.

4.2.2. Second-order TVD schemes

Second-order space-centered and upwind schemes described above are not monotonicity preserving schemes. A monotonicity preserving scheme can be obtained by limiting gradients in the Lax–Wendroff or Warming and Beam schemes.

4.2.2.1. TVD Lax–Wendroff scheme. A limited form of the Lax–Wendroff scheme [24] is given by

$$\bar{g}_\alpha(\mathbf{x}, t+\delta t) - \bar{g}_\alpha(\mathbf{x}, t) = -\delta t[\bar{g}_\alpha(\mathbf{x}, t) - \bar{g}_\alpha(\mathbf{x}-\mathbf{e}_\alpha\delta t_0, t)] - \frac{\delta t}{2}(1-\delta t)\delta^-\left[\mathbf{\Psi}\left(r^-(\mathbf{x}+\frac{1}{2}\mathbf{e}_\alpha\delta t_0, t)\right)(\bar{g}_\alpha(\mathbf{x}+\mathbf{e}_\alpha\delta t_0, t) - \bar{g}_\alpha(\mathbf{x}, t))\right] \tag{57}$$

in which the ratio r^- is defined as

$$r^-(\mathbf{x}+\frac{1}{2}\mathbf{e}_\alpha\delta t_0, t) = \frac{\bar{g}_\alpha(\mathbf{x}, t) - \bar{g}_\alpha(\mathbf{x}-\mathbf{e}_\alpha\delta t_0, t)}{\bar{g}_\alpha(\mathbf{x}+\mathbf{e}_\alpha\delta t_0, t) - \bar{g}_\alpha(\mathbf{x}, t)} \tag{58}$$

and $\mathbf{\Psi}$ is a non-linear limiting function, or a limiter, which will be defined later.

4.2.2.2. TVD Warming and Beam scheme. The TVD Warming and Beam scheme can be written as

$$\bar{g}_\alpha(\mathbf{x}, t+\delta t) - \bar{g}_\alpha(\mathbf{x}, t) = -\delta t[\bar{g}_\alpha(\mathbf{x}, t) - \bar{g}_\alpha(\mathbf{x}-\mathbf{e}_\alpha\delta t_0, t)] - \frac{\delta t}{2}(1-\delta t)\delta^-\left[\mathbf{\Psi}\left(r^+\left(\mathbf{x}-\frac{1}{2}\mathbf{e}_\alpha\delta t_0, t\right)\right)(\bar{g}_\alpha(\mathbf{x}, t) - \bar{g}_\alpha(\mathbf{x}-\mathbf{e}_\alpha\delta t_0, t))\right], \tag{59}$$

where the ratio r^+ is defined as

$$r^+\left(\mathbf{x}-\frac{1}{2}\mathbf{e}_\alpha\delta t_0, t\right) = \frac{\bar{g}_\alpha(\mathbf{x}+\mathbf{e}_\alpha\delta t_0, t) - \bar{g}_\alpha(\mathbf{x}, t)}{\bar{g}_\alpha(\mathbf{x}, t) - \bar{g}_\alpha(\mathbf{x}-\mathbf{e}_\alpha\delta t_0, t)}. \tag{60}$$

The TVD Lax–Wendroff scheme reduces to the Lax–Wendroff scheme when $\mathbf{\Psi} = 1$, and the Warming and Beam scheme when when $\mathbf{\Psi} = r$. The TVD Warming and Beam scheme behaves in the opposite way. Both the TVD Lax–Wendroff scheme and the TVD Warming and Beam scheme are on the support $(\mathbf{x} + \mathbf{e}_\alpha \delta t_0, \mathbf{x}, \mathbf{x} - \mathbf{e}_\alpha \delta t_0, \mathbf{x} - 2\mathbf{e}_\alpha \delta t_0)$. The limiter $\mathbf{\Psi}(r^\pm)$ used in the present study is the Van Leer limiter [21]:

$$\mathbf{\Psi}(r^\pm) = \frac{r^\pm + |r^\pm|}{1 + |r^\pm|}. \tag{61}$$

Basically, the TVD Lax–Wendroff scheme is identical to the TVD Warming and Beam scheme.

4.3. Discretization of body force terms

On uniform structured mesh, it is advantageous to make full use of discretization in the direction of characteristics. The directional derivative of the gradient of any variable, for instance, ψ in the $\mathbf{e}_\alpha$ direction is discretized as

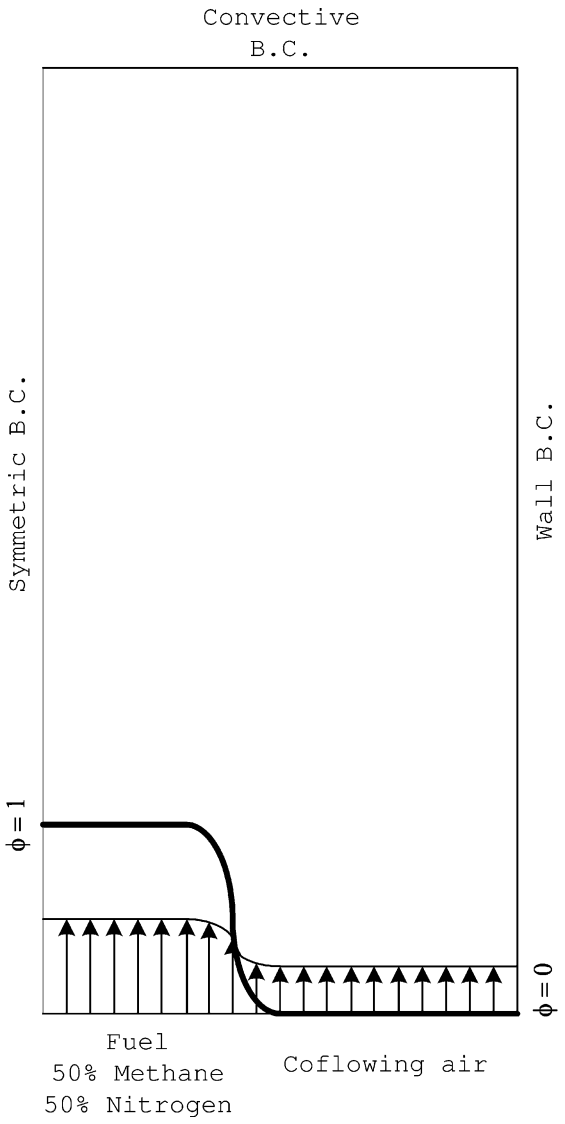

Fig. 1. Schematic representation of the computational domain and boundary conditions (not to scale).

$$\delta t_0 \mathbf{e}_\alpha \cdot \nabla \psi = \frac{\psi(\mathbf{x} + \mathbf{e}_\alpha \delta t_0) - \psi(\mathbf{x} - \mathbf{e}_\alpha \delta t_0)}{2} \tag{62}$$

in which the second-order accurate central difference is projected along characteristics. Derivatives other than the directional derivatives can be obtained by taking moments of the 1-D second-order central discretization of the first and second derivatives along characteristics for consistency, although its effect on stability is not critical. Specifically, the first derivative and the second derivative are discretized as follows [31] (see Appendixes A and B):

$$\nabla \psi = \sum_{\alpha \neq 0} \frac{t_\alpha \mathbf{e}_\alpha \cdot \hat{\mathbf{i}} [\psi(\mathbf{x} + \mathbf{e}_\alpha \delta t_0) - \psi(\mathbf{x} - \mathbf{e}_\alpha \delta t_0)]}{2 c_s^2 \delta t_0}, \tag{63}$$

$$\nabla \cdot \nabla \psi = \sum_{\alpha \neq 0} \frac{t_\alpha [\psi(\mathbf{x} + \mathbf{e}_\alpha \delta t_0) - 2\psi(\mathbf{x}) + \psi(\mathbf{x} - \mathbf{e}_\alpha \delta t_0)]}{c_s^2 \delta t_0^2}, \tag{64}$$

in which $\hat{\mathbf{i}}$ is the unit vector pointing along the i-coordinate axis. Eq. (63) appears in LBE as in the inner product with the velocity vector, which is $\mathcal{O}(Ma)$. Thus, its contribution to the overall truncation error is smaller than the directional derivatives. Eq. (64) requires modification in order to be used for discretization of the diffusion term:

$$\nabla \cdot (\rho \mathscr{D} \nabla \phi) = \sum_{\alpha} \frac{t_\alpha \left[\rho \mathscr{D}_{(\mathbf{x} + 1/2 \mathbf{e}_\alpha \delta t_0)} (\phi(\mathbf{x} + \mathbf{e}_\alpha \delta t_0) - \phi(\mathbf{x})) - \rho \mathscr{D}_{(\mathbf{x} - 1/2 \mathbf{e}_\alpha \delta t_0)} (\phi(\mathbf{x}) - \phi(\mathbf{x} - \mathbf{e}_\alpha \delta t_0)) \right]}{c_s^2}. \tag{65}$$

5. Numerical test

The numerical model is tested with the simulation of a ducted slot jet diffusion flame of Burke–Schumann [32]. The exothermic reaction of combustion yields high temperature combustion products typically around 2300 K for hydrocarbon fuels burning in air. Density variation of order of 10 can exist in the flame. Numerical

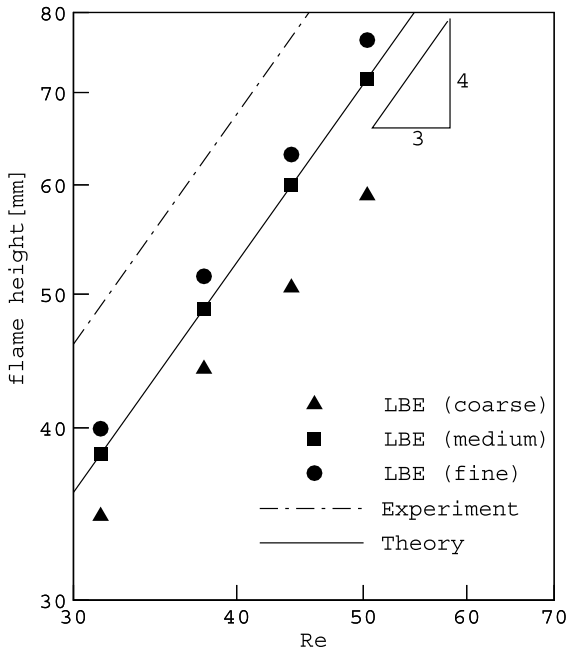

Fig. 2. Comparison of steady flame heights at various Re in logarithmic scale. Triangles denote LBE results with 125×500 grid, squares denote LBE results with 250×1000 grid, and circles denote LBE results with 500×2000 grid. Both theoretical and experimental results are from Roper [33].

simulations are carried out to reproduce the flicker frequency of buoyant jet diffusion flame. Here we introduce the following non-dimensional variables:

$$\bar{x} = \frac{x}{L_0}, \quad \bar{u} = \frac{u}{c_0}, \quad \bar{t} = \frac{t}{L_0/c_0}, \quad \bar{v} = \frac{v}{c_0 L_0}, \tag{66}$$

where L_0 and c_0 are the characteristic length and velocity, and defined as $L_0 = \delta x_0$ and $c_0 = \delta x_0/\delta t_0$, respectively. Variables with overbar are non-dimensional variables whereas variables without overbar are variables with physical dimensions.

Three systematically refined grids are used to investigate grid effect. The computational domain covers a region of $\bar{x} \in [0, 125]$ in the x direction and $\bar{y} \in [0, 500]$ in the y direction in coarse grid calculations, $\bar{x} \in [0, 250]$ and $\bar{y} \in [0, 1000]$ in medium grid calculations, and $\bar{x} \in [0, 500]$ and $\bar{y} \in [0, 2000]$ in fine grid calculations. The corresponding burner widths are $\bar{W} = 10$, $\bar{W} = 20$, and $\bar{W} = 40$. They are located at $(\bar{x}, \bar{y}) = (0, 0)$ and fuelled by 50% methane and 50% nitrogen by volume. The fuel and co-flowing air are separated by infinitely thin walls at the inflow. The schematic representation of the domain and boundaries is shown in Fig. 1. The computation uses a symmetric boundary condition for the centerline, and a bounce-back scheme to emulate no-slip and impermeable wall for the outer boundary. Equilibrium boundary conditions are imposed at the inflow and outflow nodes and prescribed macroscopic values for the inflow condition and zero normal gradients for the outflow boundary are utilized in order to evaluate the equilibrium. Still air is assumed to be the initial condition for the computational domain and the flame is located at the jet inlet. Physical width of the slot is then $W = 2$ mm and the outer walls are located at $x = -250$ mm and $x = 250$ mm, and physical height of the computational domain is $H = 1000$ mm. The velocity of the fuel stream ranges from 0.2 to 0.4 m/s with corresponding Re from 25.18 to 50.35. Re is based on the velocity of the fuel jet and the width of the slot. At this range of Re, the flame dynamics is dominated by the buoyant effects.

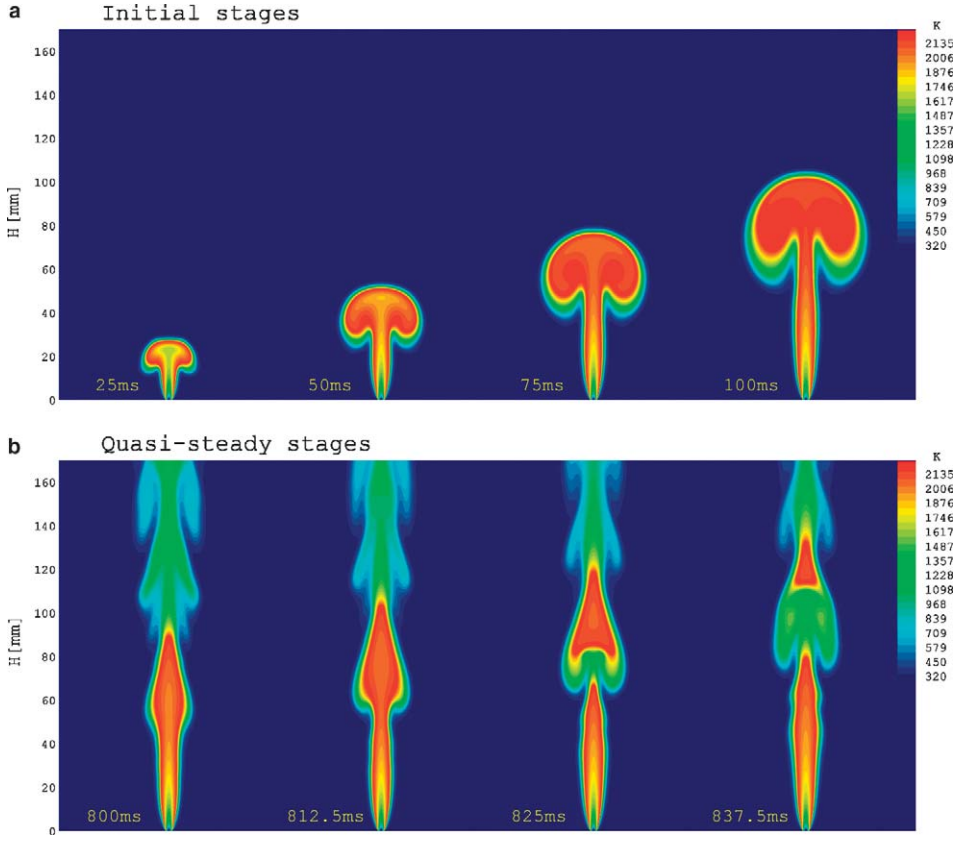

Fig. 3. Temperature contours of *quasi-incompressible* jet flame at different times: (a) initial stages right after ignition at the jet exit, (b) later stages at quasi-steady state.

To validate the present LBE model, calculated steady flame heights are compared with the theoretical results of Roper [33] in an infinitely long ducted slot geometry. We choose $D_\infty = \nu = 1.589 \times 10^{-5}$ m^2/s, $a = 0.6g(T_f/T_\infty - 1)$, $T_f = 2182.8$ K, and $T_\infty = 298$ K in Roper's correlations for the buoyancy-controlled slot burner. Since the diffusion flame model considered is inherently oscillatory and does not reach steady-state, the numerical formulation needs to be modified to yield steady-state solutions. Instead of using Eq. (25), we assume that the time derivative of density disappears at steady-state:

$$\frac{\partial \rho}{\partial t} + e_{xi}\frac{\partial \rho}{\partial x_i} \approx e_{xi}\frac{\partial \rho}{\partial x_i}. \tag{67}$$

This formulation is not generally valid, but very useful to calculate the steady flame height. The velocity of the co-flow air stream is 10% of the velocity of the fuel stream to mimic the assumptions used by Roper. Fig. 2 compares the steady flame heights calculated by the steady LBE model with the experimental and theoretical flame heights for buoyancy driven flames. The medium grid calculations are in good agreement with the fine grid calculations. Both calculations fall between the experimental and theoretical flame heights, although they favor the theoretical predictions. The slope of 4/3 is confirmed for the medium and fine grid calculations, but the results from the coarse grid calculations deviate from the slope as *Re* increases. For these reasons, the medium grid will be used in the following calculations.

In unsteady jet diffusion flames, three effects can arrive from density variation, e.g., thermal or volumetric expansion, buoyancy effects and vorticity generation [27]. The first two effects are evident as one examines the continuity and momentum equations. The non-solenoidal velocity field ($\nabla \cdot \mathbf{u}$) complicates the analysis since the incompressible fluid assumption can no longer hold. The buoyancy forces appear in the momentum equa-

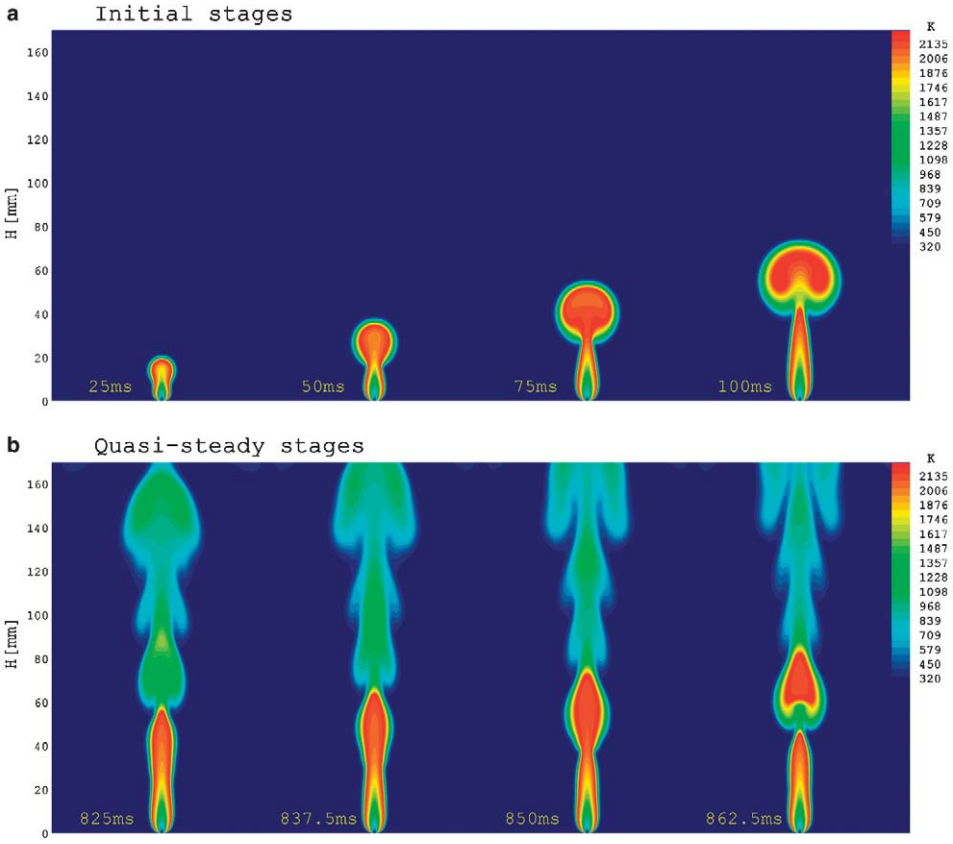

Fig. 4. Temperature contours of *incompressible* jet flame at different times: (a) initial stages right after ignition at the jet exit, (b) later stages at quasi-steady state.

tion as a source term which accelerates the flow resulting in dynamic changes in the flame structure of vertical jet diffusion flames. The dynamic change can also be seen from a Kelvin–Helmholtz type instability which is attributed to buoyancy induced shear layer around the flame and periodically occurring vortices outside the luminous flame. These vortices are buoyancy driven as shown from the numerical simulation in which outer vortices are suppressed as the gravitational acceleration is artificially set to zero. The suppression of the outer vortices yields a steady flame without the low frequency oscillation (or flame flicker) typically observed in buoyant jet diffusion flames. The flicker frequency observed in non-premixed and partially premixed flames is typically in the range of 10–20 Hz (see [35] and references therein). Buckmaster [34] measured frequencies for methane burning in air and reported that for a 2 mm circular nozzle there was a monotonic increase from 12 to 14 Hz as the mean burner exit speed was increased from 1 to 9 m/s. Sato et al. [36] found the flickering frequencies near 13 Hz for a 2 mm circular nozzle. They used C_3H_8 as fuel and varied flame heights and jet exit velocities. Generally, the frequency is relatively independent of the fuel type, nozzle size, and jet exit velocity.

Fig. 3 shows the temperature contours of the jet diffusion flame in the initial developmental stages and quasi-steady stages by the quasi-incompressible model at $Re = 50.35$ and the co-flow air stream set to the same velocity as the fuel stream. For a short time after ignition at the jet inlet (Fig. 3(a)), the flame exhibits a typical Rayleigh–Taylor type instability. Mushroom-shaped vortices induced by the Rayleigh–Taylor instability will soon be swept away. At later times, a Kelvin–Helmholtz type instability due to buoyancy induced shear layer around the flame appears and regularly occurring vortices outside the flame are observed (Fig. 3(b)). In Fig. 4, the result by the incompressible model is also presented. Generally, the flame height of the incompressible model is much smaller than that of the quasi-incompressible model. The difference between these two models originates from the term $\mathrm{d}\rho/\mathrm{d}\phi\nabla\cdot(\rho\mathscr{D}\nabla\phi)$ in Eq. (12).

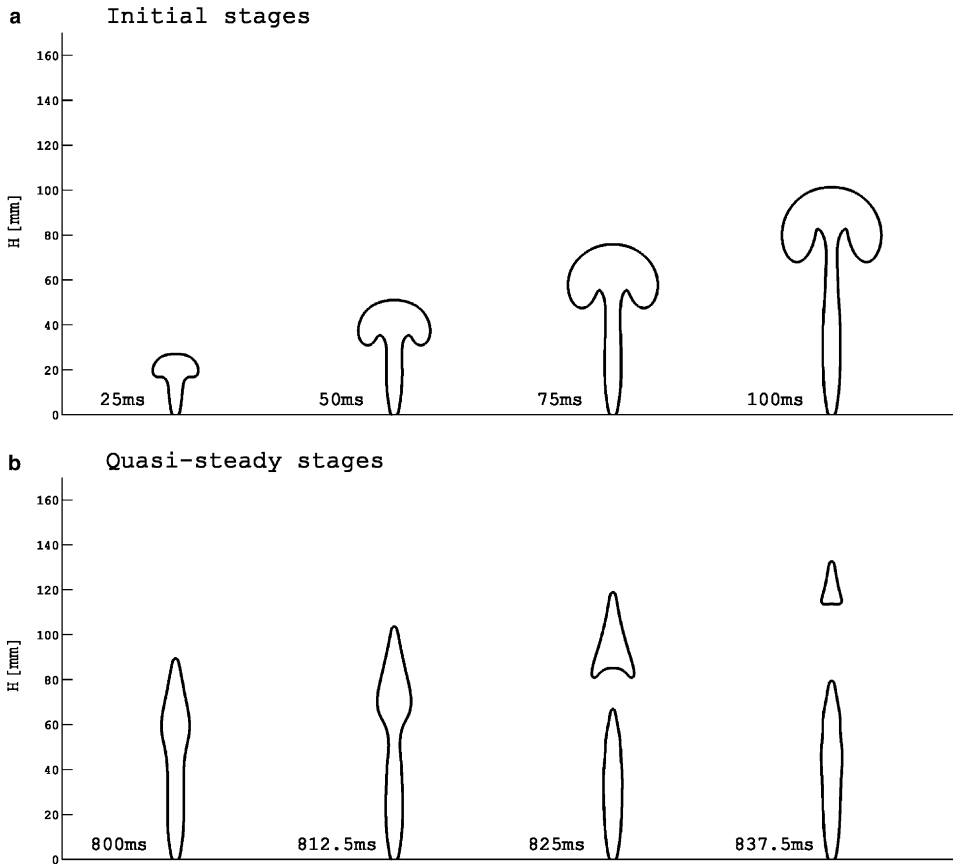

Fig. 5. Flame location represented by $\phi = \phi_{st}$ of *quasi-incompressible* jet flame at different times: (a) initial stages right after ignition at the jet exit, (b) later stages at quasi-steady state.

The term $d\rho/d\phi$ in Eq. (12) is typically positive in the fuel rich regime inside the flame envelope ($\phi_{st} < \phi < 1$) and negative in the fuel lean regime outside the flame envelope ($0 < \phi < \phi_{st}$). The volumetric expansion term becomes [27]

$$\mathbf{S}_V = -\omega(\nabla \cdot \mathbf{u}) = \omega\left(\frac{1}{\rho^2}\frac{d\rho}{d\phi}\nabla \cdot (\rho\mathscr{D}\nabla\phi)\right), \tag{68}$$

where ω is the vorticity vector. Eq. (68) states that volumetric expansion can result in vorticity generation when it has the same sign as the vorticity. An inflection point in mixture fraction exists for jet diffusion flames. As a result, vorticity generation as well as destruction can result from volumetric expansion; in specific, $\mathbf{S}/\omega < 0$ in the fuel lean regime, $\mathbf{S}/\omega > 0$ in the regime bounded by the stoichiometric contour and inflection-point contour of the fuel rich regime, and $\mathbf{S}/\omega < 0$ in the core regime.

The baroclinic effect can be evaluated following a similar approach. Assuming that the pressure gradient is due to hydrostatic pressure alone, the baroclinicity can be expressed as

$$\mathbf{S}_B = -\nabla\frac{1}{\rho}x\nabla P = -\nabla vx\nabla P = -\nabla vx\rho_\infty\mathbf{g}, \tag{69}$$

where ρ_∞ is the ambient fluid density. Employing the conserved scalar approach, one obtains the following expression for baroclinicity [27]:

$$\mathbf{S}_B = \frac{\rho_\infty}{\rho^2}\frac{d\rho}{d\phi}\nabla\phi x\mathbf{g}. \tag{70}$$

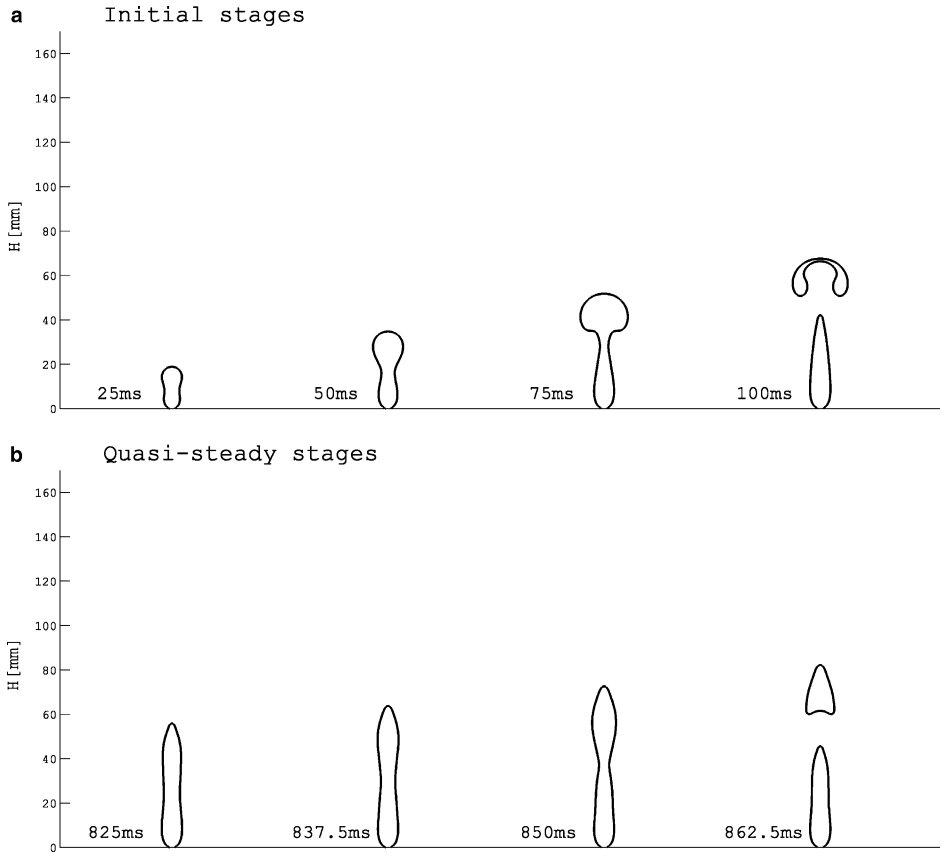

Fig. 6. Flame location represented by $\phi = \phi_{st}$ of *incompressible* jet flame at different times: (a) initial stages right after ignition at the jet exit, (b) later stages at quasi-steady state.

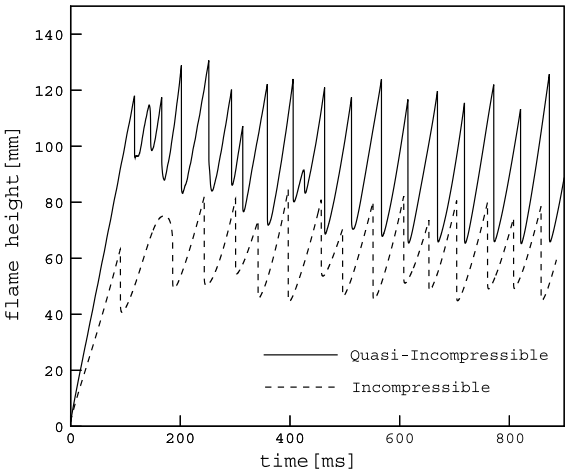

Fig. 7. Time trace of the flame height by the quasi-incompressible and the incompressible models at $Re = 50.35$.

Table 1
Flicker frequency (Hz)

Re[a]	Quasi-incompressible model	Incompressible model
25.18	18.18	11.46
37.16	19.37	12.68
50.35	19.05	20.83

[a] Based on the mean velocity of the fuel jet and the width of the slot.

The sign of $d\rho/d\phi$ is related to the baroclinicity shown above. The baroclinicity is negative in the fuel rich regime but positive in the fuel lean regime. As a result, the baroclinicity suppresses vorticity in the fuel rich regime of a jet diffusion flame, yielding laminarization effects to the flow. The baroclinicity, however, can generate vorticity in the fuel lean regime.

The flame location represented by $\phi = \phi_{st}$ is plotted in Fig. 5 for the quasi-incompressible model and in Fig. 6 for the incompressible model. Mushroom-shaped Rayleigh–Taylor type instability is clearly observed in Figs. 5(a) and 6(a). Figs. 5(b) and 6(b) roughly represent one period of flame flicker, during which time flame cutting is observed. The time evolution of the flame heights of the quasi-incompressible model and that of the incompressible model at $Re = 50.35$ is shown in Fig. 7. Sharp changes in the flame height are due to the flame cutting. In the incompressible model, contribution of volumetric expansion and the baroclinic effect are not reflected in the solution, which results in smaller flame height. Table 1 summarizes the flicker frequencies for different Re and LBE models. The flicker frequency is approximately 18–19 Hz for the quasi-incompressible model confirming the previous statement that the flicker frequency is relatively independent of the jet exit velocity. Although all the computational results are within the range of experimental and computational data [37], the incompressible model is unable to predict velocity independent flicker frequency. If gravity is set to zero computationally, flickering ceases.

6. Concluding remarks

In the present paper, we propose a two-distribution lattice Boltzmann equation (LBE) algorithm for solving the time-dependent and steady laminar diffusion flames within the context of the Burke–Schumann flame sheet model. One distribution function models the transport of the Schvab–Zeldovich coupling function, or the mixture fraction to combine the energy and species equations. Since the present derivation of the LBE is general for any unsteady advection–diffusion equations, it is equally applicable to flame calculation with a finite rate

chemistry model. The other distribution function models the quasi-incompressible Navier–Stokes equations. In the quasi-incompressible flow, the density and the temperature depend on the mixture fraction but not on the pressure, and the fluids components are assumed to be compressible only in the mixing region. An incompressible model is obtained if the linear deformation of the fluids (e.g., $\nabla \cdot \mathbf{u}$) is neglected in the derivation of the LBE.

The numerical model is tested with the simulation of a slot jet diffusion flame of Burke–Schumann. To enhance the robustness of the LBE method while retaining second-order global accuracy, the TVD Lax–Wendroff scheme is applied to the streaming step of the proposed LBE formulation. Right after ignition at the jet inlet, the Rayleigh–Taylor type instability is observed, which is swept away by convection. At later times, the Kelvin–Helmholtz type instability develops due to the presence of the buoyancy induced shear layer around the flame. Numerical simulation successfully reproduces the flicker frequency of buoyant jet diffusion flame. We also compare the quasi-incompressible model with the incompressible model. Vorticity generation as well as destruction can result from the volumetric expansion. In the incompressible model, contribution of volumetric expansion is not captured in the solution resulting in a much smaller flame height.

Future work might include flame simulation of finite rate chemistry. Two-distribution LBE algorithm can still be used for the mass and momentum, and energy transport equations. The species transport equations can be solved by either the LBE algorithm developed in Section 3.3 with the addition of source terms or the conventional numerical approaches. Development of a monotonicity preserving LBE method on unstructured meshes is urgent for practical applications. The multiple-relaxation-time model (for instance, see [38]) would further stabilize the present single-relaxation-time model at the cost of slight increase in computation time and memory.

Acknowledgments

T. Lee and C.-L. Lin acknowledge support from the Carver Scientific Research Initiative Grants Program at the University of Iowa. The partial support of the IIHR – Hydroscience & Engineering at the University of Iowa is also acknowledged. L.-D. Chen acknowledges support from NASA Microgravity Science, Grant No. NCC3-666, under the technical management of D.P. Stocker and M.K. King.

Appendix A

If we assume that the thermodynamic pressure $p^{(t)}$ is constant, the ideal gas EOS can be written for the mixture density

$$\rho = \frac{p^{(t)} MW_m}{R_u T} = \frac{p^{(t)}}{R_u T \sum_i Y_i / MW_i}, \tag{A.1}$$

where MW_i is the molecular weight of species i and R_u the universal gas constant. Multiplying the mixture fraction ϕ to the above equation, it yields

$$\rho\phi = \frac{p^{(t)}\phi}{R_u T \sum_i Y_i / MW_i}. \tag{A.2}$$

Given $\rho\phi$ from Eq. (48), the mixture fraction ϕ can be calculated by solving a quadratic equation. For $0 \leqslant \rho\phi < \rho_{st}\phi_{st}$,

$$\rho\phi = \frac{p^{(t)}\phi}{R_u\left(\frac{1}{MW_{st}}\frac{\phi}{\phi_{st}} + \frac{1}{MW_{O_\infty}}\frac{\phi_{st}-\phi}{\phi_{st}}\right)\left(\frac{T_{st}-T_{O_\infty}}{\phi_{st}}\phi + T_{O_\infty}\right)} \tag{A.3}$$

which can be solved for $0 \leqslant \phi < \phi_{st}$. For $\rho_{st}\phi_{st} < \rho\phi \leqslant \rho_{O_\infty}$

$$\rho\phi = \frac{p^{(t)}\phi}{R_u\left(\frac{1}{MW_{st}}\frac{1-\phi}{1-\phi_{st}} + \frac{1}{MW_{F_\infty}}\frac{\phi-\phi_{st}}{1-\phi_{st}}\right)\left(\frac{T_{F_\infty}-T_{st}}{1-\phi_{st}}(\phi-1) + T_{F_\infty}\right)} \tag{A.4}$$

which can be solved for $\phi_{st} < \phi \leqslant 1$.

Appendix B

We consider a model advection equation for a scalar variable f with a source term Q.

$$\frac{\partial f}{\partial t} + \mathbf{e}\cdot\nabla f + Q = 0, \tag{B.1}$$

where $\mathbf{e}$ is the advection velocity. We expand the variable f by a Taylor series in time, retaining terms of the second order, giving in the interval δt, and obtain

$$f^{n+1} = f^n + \delta t \left.\frac{\partial f}{\partial t}\right|_n + \frac{\delta t^2}{2}\left.\frac{\partial^2 f}{\partial t^2}\right|_n. \tag{B.2}$$

From Eq. (B.1), we can write

$$\left[\frac{\partial f}{\partial t}\right]_n = -[\mathbf{e}\cdot\nabla f + Q]_n \tag{B.3}$$

and differentiate it to obtain

$$\left[\frac{\partial^2 f}{\partial t^2}\right]_n = -\frac{\partial}{\partial t}[\mathbf{e}\cdot\nabla f + Q]_n. \tag{B.4}$$

The above equations can also be written as

$$\frac{\partial}{\partial t}(\mathbf{e}\cdot\nabla f) = \mathbf{e}\cdot\nabla\left(\frac{\partial f}{\partial t}\right) = -\mathbf{e}\cdot\nabla(\mathbf{e}\cdot\nabla f + Q) \tag{B.5}$$

and

$$\frac{\partial Q}{\partial t} = \frac{\partial Q}{\partial f}\frac{\partial f}{\partial t} = -S(\mathbf{e}\cdot\nabla f + Q) \tag{B.6}$$

with $S \equiv \partial Q/\partial f$.

We can therefore approximate Eq. (B.2) as

$$f^{n+1} - f^n = \delta t[\mathbf{e}\cdot\nabla f + Q]_n + \frac{\delta t^2}{2}[\mathbf{e}\cdot\nabla(\mathbf{e}\cdot\nabla f + Q) + S(\mathbf{e}\cdot\nabla f + Q)]_n + \mathrm{O}(\delta t^3). \tag{B.7}$$

Omitting the effect of S [39], we have

$$f^{n+1} - f^n = \delta t[\mathbf{e}\cdot\nabla f + Q]_n + \frac{\delta t^2}{2}\mathbf{e}\cdot\nabla[\mathbf{e}\cdot\nabla f + Q]_n \tag{B.8}$$

which is second-order accurate in time and conditionally stable.

If f represents the particle distribution function f_α, Eq. (B.8) can be projected along characteristics up to second-order accuracy as follows [19]:

$$f_\alpha(\mathbf{x} + \mathbf{e}\delta t, t + \delta t) - f_\alpha(\mathbf{x}, t) = \frac{\delta t}{2}[Q(\mathbf{x} + \mathbf{e}\delta t, t) + Q(\mathbf{x}, t)] \tag{B.9}$$

while the Crank–Nicolson discretization of Eq. (B.1) along characteristics yields

$$f_\alpha(\mathbf{x} + \mathbf{e}\delta t, t + \delta t) - f_\alpha(\mathbf{x}, t) = \frac{\delta t}{2}[Q(\mathbf{x} + \mathbf{e}\delta t, t + \delta t) + Q(\mathbf{x}, t)]. \tag{B.10}$$

Therefore, the explicit treatment of the source term in the LBE formulation can be still second-order accurate if the source term is not directly dependent on the particle distribution function. However, unconditional stability of the Crank–Nicolson discretization is lost. Note that the following explicit formulation is always first-order accurate:

$$f_\alpha(\mathbf{x} + \mathbf{e}\delta t, t + \delta t) - f_\alpha(\mathbf{x}, t) = \delta t Q(\mathbf{x}, t). \tag{B.11}$$

References

[1] S. Chen, G.D. Doolen, Lattice Boltzmann method for fluid flows, Annu. Rev. Fluid Mech. 30 (1998) 329.
[2] X. Nie, G.D. Doolen, S. Chen, Lattice-Boltzmann simulations of fluid flows in MEMS, J. Stat. Phys. 107 (2002) 279.
[3] S. Succi, G. Bella, F. Papetti, Lattice kinetic theory for numerical combustion, J. Sci. Comput. 12 (4) (1997) 395.
[4] K. Yamamoto, X. He, G.D. Doolen, Simulation of combustion field with lattice Boltzmann method, J. Stat. Phys. 107 (2002) 367.
[5] Q. Zou, S. Hou, S. Chen, G.D. Doolen, An improved incompressible lattice Boltzmann model for time-independent flows, J. Stat. Phys. 81 (1995) 35.
[6] X. He, L.-S. Luo, Lattice Boltzmann model for the incompressible Navier–Stokes equation, J. Stat. Phys. 88 (1997) 927.
[7] O. Filippova, D. Hänel, Lattice-BGK model for low Mach number combustion, Int. J. Mod. Phys. C 9 (8) (1998).
[8] O. Filippova, D. Hänel, A novel lattice BGK approach for low Mach number combustion, J. Comput. Phys. 158 (2000) 139.
[9] Y.-H. Qian, D. d'Humieres, P. Lallemand, Lattice BGK models for Navier–Stokes equation, Europhys. Lett. 17 (1992) 479.
[10] J.-C. Sheu, L.-D. Chen, Higher-order numerical model for simulation of time-dependent variable-density flows, AIAA 34 (1996) 2090.
[11] X. He, X. Shan, G.D. Doolen, A discrete Boltzmann equation model for non-ideal gases, Phys. Rev. E 57 (1998) R13.
[12] X. He, S. Chen, R. Zhang, A lattice Boltzmann scheme for incompressible multiphase flow and its application in simulation of Rayleigh–Taylor instability, J. Comput. Phys. 152 (1999) 642.
[13] M.S. Day, J.B. Bell, Numerical simulation of laminar reacting flows with complex chemistry, Combust. Theory Modelling 4 (4) (2000) 535.
[14] J. Lowengrub, L. Truskinovsky, Quasi-incompressible Cahn–Hilliard fluids and topological transitions, Proc. R. Soc. Lond. A 454 (1998) 2617.
[15] T. Lee, C.-L. Lin, A pressure evolution lattice Boltzmann equation method for two-phase flow with phase change, Phys. Rev. E 67 (2003) 056703.
[16] P.D. Lax, B. Wendroff, Systems of conservation laws, Commun. Pure Appl. Math. 13 (1960) 217.
[17] G.R. McNamara, A.L. Garcia, B.J. Alder, Stabilization of thermal lattice Boltzmann models, J. Stat. Phys. 81 (1995) 395.
[18] R. Zhang, H. Chen, Y.H. Qian, S. Chen, Effective volumetric lattice Boltzmann scheme, Phys. Rev. E 63 (2001) 056705.
[19] T. Lee, C.-L. Lin, An Eulerian description of the streaming process in the lattice Boltzmann equation, J. Comput. Phys. 185 (2) (2003) 445.
[20] R.F. Warming, R.W. Beam, Upwind second order difference schemes and applications in aerodynamic flows, AIAA J. 24 (1976) 1241.
[21] B. Van Leer, Towards the ultimate conservative difference scheme. II. Monotonicity and conservation combined in a second order scheme, J. Comput. Phys. 14 (1974) 361.
[22] C. HirschNumerical Computation of Internal and External Flows, vol. II, Wiley, New York, 1990.
[23] S. Teng, Y. Chen, H. Ohashi, Lattice Boltzmann simulation of multiphase fluid flows through the total variation diminishing with artificial compression scheme, Int. J. Heat Fluid Flow 21 (2000) 112.
[24] P.L. Roe, Generalized formulation of TVD Lax–Wendroff schemes, ICASE Report 84-53, NASA CR-172478, NASA Langley Research Center, 1984.
[25] S.R. Turns, An Introduction to Combustion, McGraw-Hill, New York, 2000.
[26] R.W. Bilger, Turbulent jet diffusion flames, Prog. Energy Combust. Sci. 1 (1976) 87.
[27] L.-D. Chen, W.M. Roquemore, L.P. Goss, V. Vilimpoc, Vorticity generation in jet diffusion flames, Combust. Sci. Tech. 177 (1991) 41.
[28] Y.-H. Qian, S.-Y. Chen, Dissipative and dispersive behavior of lattice-based models for hydrodynamics, Phys. Rev. E 61 (2000) 2712.
[29] S.P. Dawson, S. Chen, G.D. Doolen, Lattice Boltzmann computations for reaction–diffusion equations, J. Chem. Phys. 98 (1993) 15.
[31] T. Lee, C.-L. Lin, A stable discretization of the lattice Boltzmann equation method for simulation of incompressible two-phase flows at high density ratio, J. Comput. Phys. 206 (2005) 16.
[32] S.P. Burke, T.E.W. Schumann, Diffusion flames, Ind. Eng. Chem. 20 (1928) 998.
[33] F.G. Roper, The prediction of laminar jet diffusion flame sizes: part I. Theoretical model, Combust. Flame 21 (1977) 681.
[34] J. Buckmaster, The infinite candle and its stability-a paradigm for flickering diffusion flamesTwenty-First Symposium on Combustion, The Combustion Institute, 1986, p. 1829.
[35] L.-D. Chen, J.P. Seaba, W.M. Roquemore, L.P. Goss, Buoyant diffusion flamesTwenty-Second Symposium on Combustion, The Combustion Institute, 1988, p. 677.
[36] F. Sato, K. Amagai, M. Arai, Diffusion flames and their flickering motions related with Froude numbers under various gravity levels, Combust. Flame 123 (2000) 107.
[37] L.-D. Chen, V. Vilimpoc, L.P. Goss, R.W. Davis, E.F. Moore, The evolution of a buoyant jet diffusion flameTwenty-Fourth Symposium on Combustion, The Combustion Institute, 1992, p. 303.
[38] D. d'Humières, I. Ginzburg, M. Krafczyk, P. Lallemand, L.-S. Luo, Multiple-relaxation-time lattice Boltzmann models in three dimensions, Philos. Trans. R. Soc. Lond. A 360 (2002) 437.
[39] O.C. Zienkiewicz, R.L. Taylor, The Finite Element Method, McGraw-Hill, New York, 1991.